Mapping the periphery of deformation in the $A \sim 80$ region: A study of ^{83}Nb

S. M. Fischer*
Department of Physics, DePaul University, Chicago, Illinois 60614, USA and Physics Division, Argonne National Laboratory, Argonne, Illinois 60439, USA

C. J. Lister, M. P. Carpenter, N. J. Hammond, R. V. F. Janssens, E. F. Moore, G. Mukharjee, D. Seweryniak, and S. Sinha
Physics Division, Argonne National Laboratory, Argonne, Illinois 60439, USA

S. J. Freeman
Schuster Laboratory, University of Manchester, Manchester M13 9PL, United Kingdom

J. Carney
Department of Physics, DePaul University, Chicago, Illinois 60614, USA

D. P. Balamuth
Department of Physics and Astronomy, University of Pennsylvania, Philadelphia, Pennsylvania 19104, USA

Y. Sun
Department of Physics and Joint Institute for Nuclear Astrophysics, University of Notre Dame, Notre Dame, Indiana 46556, USA; Department of Physics, Tsinghua University, Beijing 100084, People's Republic of China; and Department of Physics, Xuzhou Normal University, Xuzhou, Jiangsu 221009, People's Republic of China
(Received 31 October 2006; published 18 June 2007)

^{83}Nb has been studied in order to locate the upper extent of large deformation in the $N \sim Z \sim 40$ region and ascertain its sign and magnitude. The decay scheme has been considerably extended by studying gamma decay following the ^{58}Ni(^{28}Si, $p2n$)^{83}Nb reaction at 204 and 215 MeV and using Gammasphere. Both signature partners of two rotational bands have been observed. The band properties support a $I^{\pi} = \frac{5}{2}^{+}$ ground state spin assignment. The in-band branching ratios and multipole mixing ratios were found to be consistent with significant prolate deformation, as found in other $N = 42$ isotones. The bands are particularly similar to the isotone ^{81}Y. A projected shell model analysis has been performed which provides good reproduction of the features of both bands. The calculations indicate the nucleus to be nearly axially symmetric. ^{82,83}Nb may be the heaviest nuclei in the $A \sim 80$ region with large deformation. The deformation is predicted to fall in heavier systems approaching ^{100}Sn. The conditions appear to be right for the occurrence of K isomers.

DOI: 10.1103/PhysRevC.75.064310 PACS number(s): 27.50.+e, 23.20.Lv, 23.20.En, 21.10.Re

I. INTRODUCTION

In nuclei, a low level density at the Fermi surface leads to a large negative "shell correction energy" and thus unusually strong binding. This is true for both spherical nuclei, for example ^{90}Zr$_{50}$ [1], and for highly deformed nuclei, like ^{80}Zr$_{40}$ [2]. In $N = Z$ nuclei this effect is very apparent, as both protons and neutrons have the same Fermi level, so can find a mutual shape which simultaneously has low level density and thus has unusually strong binding. This low level density situation is satisfied near particle number 39, where the nuclei have some of the most prolate-deformed ground states known, with $\varepsilon_2 \sim 0.4$ [3,4], and the extra binding energy leads to ^{76,77}Y [5,6] forming a promontory of bound nuclei sticking out from the proton drip line, where the neighboring drip line odd-Z nuclei are particle-decay unstable. Raising or lowering the Fermi level away from the shell gaps quenches the deformation, although the detailed shape changes are very sensitive to the exact level sequence near the Fermi surface. Below particle number 39 many nuclei have been studied in the last decade, and the quenching is quite well categorized. For heavier $N \sim Z$ nuclei the situation is far less clear. A rather sharp transition from deformed to near-spherical nuclei has been predicted [7,8] once the Fermi level is above the $Z = 40$ gap, and the limited data [9–12] support this view. Above ^{80}Zr the drip line has been located following fragmentation studies and the very fast superallowed decays from odd-odd nuclei have been observed [5,13]. The Legnaro and Göttingen groups have successfully used particle-γ coincidence spectroscopy to investigate proton-rich molybdenum and ruthenium isotopes [10–12,14]. The Stockholm group has also explored this region and found superdeformed bands in several nuclei [15,16]. Isomers have been found in niobium and technetium nuclei [17,18], though their spins, excitation energies, and structure have yet to be identified. One clear case that has been pointed out [19] to be near the upper boundary of substantial deformation is the $N = Z + 1$ nucleus $^{83}_{41}$Nb$_{42}$.

The structure of these heavy $N \sim Z$ nuclei, particularly the occurrence of low-lying shape isomers, is important in

*sfischer@depaul.edu

determining the rate and extent of the rp-process nucleosynthesis [20–22]. However, apart from the original observation of excited states in ^{83}Nb [19], no further experimental work mapping these $N \sim Z$ deformed nuclei has been reported. We have reinvestigated ^{83}Nb; experimentally extending the spectrum of excited states to delineate the rotational band structure and measuring angular distributions to extract the sign of the deformation. Theoretically, we have used the projected shell model [23,24] in order to better understand the high mass side of the deformed region.

II. THE EXPERIMENT

^{83}Nb nuclei were produced following the ^{28}Si(^{58}Ni, $p2n$) reaction at 204 MeV and 215 MeV. The ^{58}Ni beams were delivered by the ATLAS accelerator at Argonne National Laboratory. Gamma rays emitted in the reaction were detected by the Gammasphere array [25], comprised of 95 Compton-suppressed hyperpure Ge detectors. The recoiling nuclei passed through the Argonne Fragment Mass Analyzer (FMA) [26] and were separated according to their ratio of mass to charge. The slits at the exit of the FMA were narrowed to allow only recoils of $A = 83$ to reach the focal plane detectors, which consisted of two position-sensitive channel plate detectors followed by an ionization chamber. The channel plate detectors determined the position and arrival time of the recoils, which were then stopped in the ionization chamber filled with isobutane gas at a pressure of ~20 torr. Charge was collected from three segments of the ionization chamber in order to determine the energy loss of the recoils through the chamber. Z-identification was achieved by considering the energy loss of the recoils in the first two segments of the ionization chamber (ΔE) versus the total energy ($E_{\rm tot}$) deposited in the detector. The event trigger required a coincidence between a clean γ ray detected in Gammasphere and a channel plate signal. Due to the inverse kinematics of the reaction, the channel plate (focal plane) signals consisted of both recoiling nuclei and some scattered beam. Data were collected at two different beam energies. The 215 MeV data were obtained over a time period of approximately 17 hours, using a 188 μg/cm^2 ^{28}Si target, and a typical beam current of 10 pnA. The 204 MeV data were obtained using the equivalent of a 360 μg/cm^2 ^{28}Si target, and a typical beam current of 7.5 pnA for approximately 22 hours. No significantly different features were found in the two data sets, and the data were combined for portions of the final analysis. The study by Gross *et al.* [19] used the same reaction with a beam energy of 195 MeV and reported a production cross section for ^{83}Nb of 180(80) μb. Figure 1 exemplifies the small cross section for producing ^{83}Nb relative to other $A = 83$ reaction channels and also the sensitivity of the recoil separator technique. A spectrum of all γ rays detected in coincidence with $A = 83$ recoils is displayed in the upper panel, while the lower panel shows the spectrum of γ rays obtained with the additional requirement that $Z = 41$. Because nuclei with different atomic numbers were not perfectly separated in the ΔE versus $E_{\rm tot}$ data from the ionization chamber, it was also necessary to subtract the γ rays from nuclei produced in the $3p$ ($Z = 39$) and $2pn$

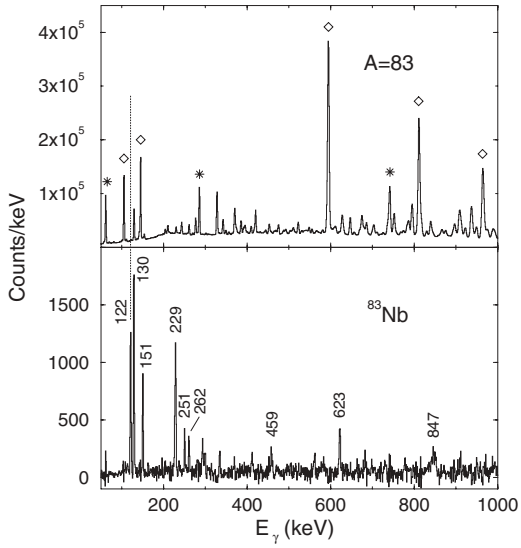

FIG. 1. An illustration of the need for both mass and atomic number gating. The upper panel shows γ rays in coincidence with $A = 83$, selected by the Fragmant Mass Analyzer. Gamma rays from the $3p$ reaction channel (^{83}Y) are marked by diamond symbols, and those from the $2pn$ channel (^{83}Zr) are marked by asterisks. The lower panel has the additional requirement of large energy loss, ΔE, in the ion chamber which causes enhancement of $Z = 41$ events.

($Z = 40$) channels in order to produce the spectrum shown in the lower panel.

III. DATA ANALYSIS

Data collected at the two beam energies were initially analyzed separately, as the energy loss behavior of the recoils in the ionization chamber is dependent on the incident energy of the recoils, which is dependent on the beam energy. For each data set, windows on recoils of $A = 83$ and $Z = 39$, 40, and 41 were optimized to include the maximum fraction of ^{83}Nb while also producing the clean selection of ^{83}Y and ^{83}Zr events for the necessary channel subtraction. The data also included events from ^{80}Sr produced in the $\alpha 2p$ channel and accepted by the FMA due to an ambiguity in the mass-to-charge ratio. Gamma ray events correlated with ^{83}Nb were required to have a well-defined time relationship between Gammasphere and the channel plate data, a recoil detected in the appropriate window of the ΔE versus $E_{\rm tot}$ histogram, and to survive the application of mass subtraction, if necessary. Doppler corrections were applied to the γ-ray energies on an event-by-event basis, with v/c depending on the measured total energy of the recoil deposited in the ionization chamber, as determined from the data for ^{83}Y. For the 204 MeV data, the value of v/c varied from approximately 0.054 to 0.060 depending on $E_{\rm tot}$ of the recoil. Singles γ-ray spectra were produced for ^{83}Nb from the data at both energies. The spectra were added together to enhance statistics. The mass- and Z-gated data were also sorted into γ-γ coincidence matrices. Analysis of these data allowed for the identification of additional transitions not observed in the singles spectrum, and for the placement of transitions in the energy level scheme. The energies and relative intensities for

TABLE I. The excited states of ^{83}Nb, and their proposed spins and parities. Also given are the energies, relative intensities and measured multipolarities and mixing ratios of transitions from these states.

E_x (keV)	I_i^π	I_f^π	E_γ (keV)	I_γ	Multipoles	δ
0.0	$\frac{5}{2}^+$					
129.5(2)	$\frac{7}{2}^+$	$\frac{5}{2}^+$	129.5(2)	100(5)	$M1/E2$	+0.20(7)
229.0(2)	$\frac{3}{2}^-$	$\frac{5}{2}^+$	229.0(2)	114(6)[a]	$E1$	
251.2(2)	$\frac{9}{2}^+$	$\frac{7}{2}^+$	121.6(2)	71(3)	$M1/E2$	+0.15(6)
		$\frac{5}{2}^+$	251.2(2)	28(4)[b]	$E2$	
379.9(3)	$\frac{5}{2}^-$	$\frac{3}{2}^-$	150.9(2)	45(3)	$M1/E2$	+0.14(9)
		$\frac{7}{2}^+$	250.6(5)	<10[c]		
641.4(3)	$\frac{7}{2}^-$	$\frac{5}{2}^-$	261.5(3)	27(5)	$M1/E2$	+0.19(17)
		$\frac{3}{2}^-$	412.4(4)	26(7)		
709.9(4)	$\frac{11}{2}^+$	$\frac{9}{2}^+$	458.8(3)	26(7)		
		$\frac{7}{2}^+$	580(1)	30(16)		
873.8(3)	$\frac{13}{2}^+$	$\frac{11}{2}^+$	163.4(4)	5(3)		
		$\frac{9}{2}^+$	622.7(3)	78(10)	$E2$	
941.5(5)	$(\frac{9}{2}^-)$	$\frac{7}{2}^-$	299.8(4)	17(5)		
		$\frac{5}{2}^-$	561.9(5)	29(9)		
1325(6)	$(\frac{11}{2}^-)$	$(\frac{9}{2}^-)$	384(1)	<8		
		$\frac{7}{2}^-$	683.6(5)	25(10)		
1441.2(7)	$(\frac{15}{2}^+)$	$\frac{11}{2}^+$	731.3(5)	25(10)		
1721.0(5)	$(\frac{17}{2}^+)$	$\frac{13}{2}^+$	847.2(4)	72(14)		
1721.1(8)	$(\frac{13}{2}^-)$	$(\frac{9}{2}^-)$	779.6(6)	28(11)		
2236(1)	$(\frac{15}{2}^-)$	$(\frac{11}{2}^-)$	911(1)	18(9)		
2484(2)	$(\frac{19}{2}^+)$	$(\frac{15}{2}^+)$	1043(2)	16(9)		
2689(1)	$(\frac{17}{2}^-)$	$(\frac{13}{2}^-)$	968(1)	21(11)		
2777.4(7)	$(\frac{21}{2}^+)$	$(\frac{17}{2}^+)$	1056.4(5)	32(8)		
4009(2)	$(\frac{25}{2}^+)$	$(\frac{21}{2}^+)$	1232(2)	53[d]		
5241(3)	$(\frac{29}{2}^+)$	$(\frac{25}{2}^+)$	1232(2)	53[d]		
6664(4)	$(\frac{33}{2}^+)$	$(\frac{29}{2}^+)$	1423(2)	8		

[a]Intensity includes a contribution from a contaminant transition in ^{84}Nb.
[b]Transition is tentative.
[c]Includes the intensity of the 250.6 keV tentative transition.
[d]Energy and intensity are for the unresolved doublet.

the observed transitions in ^{83}Nb are provided in Table I. Where possible, intensities were determined from the singles data, while the intensities of weaker transitions were necessarily obtained from the coincidence data. Efficiency corrections were applied from data collected using standard γ-ray sources. Our data confirm the placement of each of the transitions previously reported by Gross *et al.* [19], and we propose 16 new transitions. The resulting level scheme is shown in Fig. 2.

The ground state band has been extended to a tentative spin of $I = \frac{33}{2}$. Our new decay scheme includes a sequence of two transitions with energies identical to within the observed resolution of the detectors. The upper panel of Fig. 3 shows transitions in the positive parity bands, and was produced by adding together the γ-ray spectra obtained by gating on the 122- and 130-keV transitions for the data at both beam energies.

The spacing and intensity pattern typical of a rotational band can be seen for the 623–847–1056 keV sequence of transitions belonging to the ground state band. The 1232 keV γ ray appears to be the next transition, but has a relative intensity of 53(13), greater than the value of 32(8) obtained for the 1056 keV γ ray. We also observe a γ ray of energy 1423 keV with a relative intensity of 8(5) that belongs to this sequence. The proposed doublet nature of the 1232 keV transition and the ordering of the γ rays within the band are based on the observed coincidence relationships and intensities. Gamma-ray transitions in the negative parity bands are indicated in the lower panel of Fig. 3. This spectrum was produced by summing together spectra gated on the 151- and 229-keV transitions for

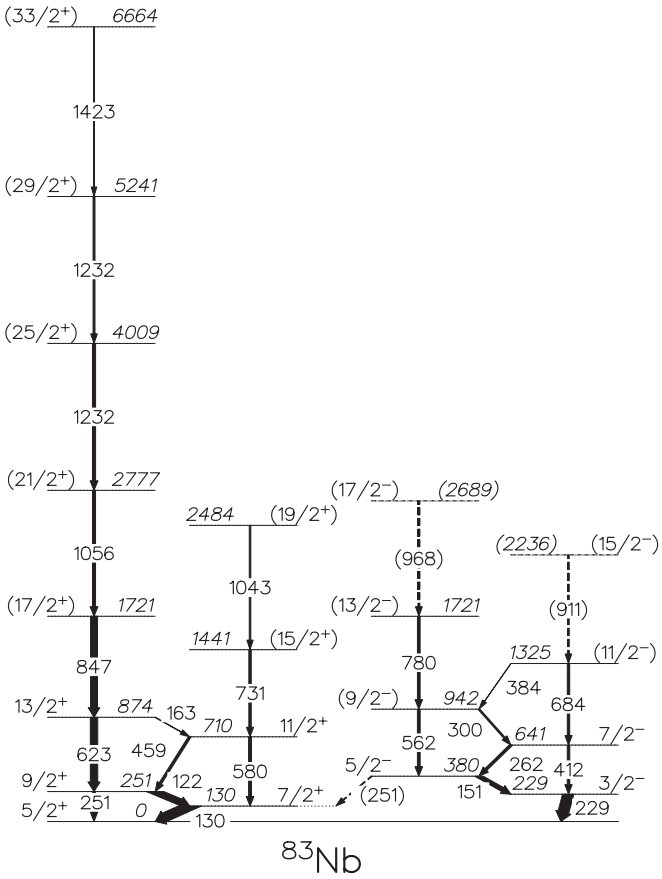

FIG. 2. The decay scheme inferred in this work. The states below 900 keV were observed previously by Gross *et al.* [19], from which a well-developed band structure has emerged.

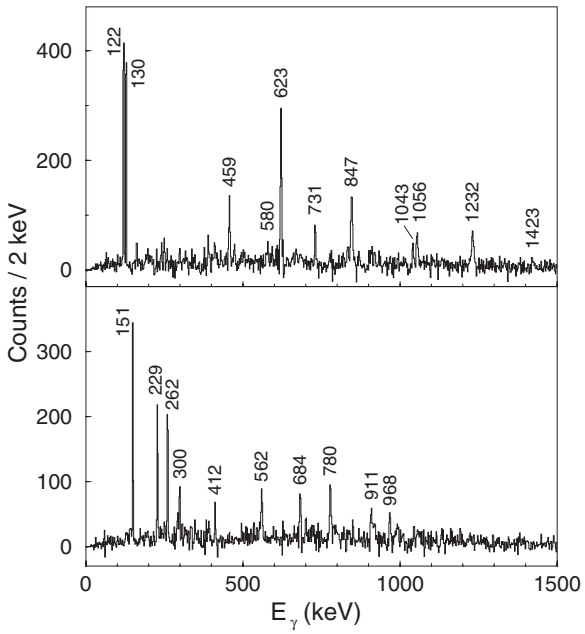

FIG. 3. γ-γ coincidence spectra for bands in ^{83}Nb. The upper panel illustrates the positive parity band; the lower panel shows transitions in the negative parity sequence.

the data from both beam energies. Individual gates on the 780 keV and 684 keV γ rays were limited in statistics, making the definite placement of the 968 keV and 911 keV γ rays above them not possible. The existence of interband transitions between the two negative parity partners also makes it difficult to determine to which bands the 968 keV and 911 keV transitions belong to. Because of this ambiguity, the placement of these γ rays is indicated as tentative in Fig. 2.

The ground state angular momentum and parity of ^{83}Nb have not been measured directly. The ^{83}Nb β-decay study by Kuroyanagi *et al.* [27] reported a half-life of 4.1(3) s, and found evidence for decay to the $\frac{7}{2}^+$77.0 keV isomeric state of ^{83}Zr. From this observation, and from the known systematics of the odd-A Nb nuclei, $\frac{9}{2}^+$ was suggested [27] as the probable spin and parity of the ground state. Gross *et al.* [19] used the same information to infer $I^\pi = (\frac{5}{2}, \frac{7}{2}, \frac{9}{2})^+$ as most probable for the parent (ground) state of the beta decay of ^{83}Nb. However, based on comparisons of the level scheme for ^{83}Nb with neighboring $N = 41$ nuclei, Gross *et al.* proposed [19] $I^\pi = \frac{5}{2}^+$ for the ground state. The extensions of the bands in this work, the in-band angular distributions, and the calculations we present in Sec. IV all support this assignment, which we now consider firm. Gamma-ray angular distributions have been analyzed, when possible, to determine the multipole character of the observed transitions. Due to the low statistics, data from detectors in nearby and complementary angles were combined in the analysis. The data at the two beam energies were initially studied separately, and then added together after no significant difference in the respective alignments was found. The results are presented in Table I, where the most probable electromagnetic character for the transitions is indicated along with the measured ($E2/M1$) mixing ratios, δ, [28] where relevant.

The well-developed band structure found in ^{83}Nb provides a framework to extract quantitative information about the sign (prolate or oblate) and size of the deformation. The multipole mixing ratios, δ, extracted from angular distributions are sensitive to both the sign and size of deformation, but have quite large uncertainties arising from limited counting statistics in each angle bin. Alternately, branching ratios that are obtained from data integrated over all angles are statistically better, but are dependent only on δ^2, thus yield only $|\delta|$ [29]. The determination of $|\delta|$ from branching ratios in a band is sensitive to K, the projection of the angular momentum on the symmetry axis, which is assumed to be spin-independent in the strong coupling limit. This is seldom exactly true in the $A \sim 80$ deformed region, due to the high rotational frequencies, and changes in alignment along the deformation axis can modify the inferred electromagnetic properties and deformation. To get from the experimental observable, δ, to deformation, the spin and magnetic moment of the band are needed [30]. The moments can be reliably calculated from the Nilsson model, or from the deformed Woods-Saxon model, using a nucleon spin g_s factor quenched by a factor of 0.7 and a rotational g-factor $g_R = \frac{Z}{A}$, or they can be empirically extracted from measured ground state magnetic moments measured in this region. We compared calculated (g_K-g_R) factors from Nilsson's original paper [31], from a more recent Nilsson calculation with "tuned" parameters [32], from a

TABLE II. Transitional quadrupole moments extracted from angular distributions and from in-band branching ratios. Gamma-ray energies are in keV, quadrupole moments in eb. ($1\ e\text{b} = 100\ e\,\text{fm}^2$). The branching ratio in column six is the ratio of $I_\gamma(\Delta I = 1)/I_\gamma(\Delta I = 2)$. The quadrupole moments in column eight are inferred assuming that the projection of the angular momentum on the symmetry axis, K, is constant and the same as the band head, as discussed in the text.

E_x (keV)	I_i^π	I_f^π	$E_\gamma(\Delta I = 1)$	δ	Branch	$\lvert\delta\rvert$	Q (eb)
130	$\frac{7}{2}^+$	$\frac{5}{2}^+$	130	+0.20(7)			+5.5(1.9)
251	$\frac{9}{2}^+$	$\frac{7}{2}^+$	122	+0.15(6)			+5.7(2.3)
251	$\frac{9}{2}^+$				2.5(4)	0.18(2)	6.8(0.8)
710	$\frac{11}{2}^+$				0.9(5)	0.9(5)	11(6)
874	$\frac{13}{2}^+$				0.06(4)	0.13(5)	5(2)
380	$\frac{5}{2}^-$	$\frac{3}{2}^-$	151	+0.14(9)			+3.2(2.0)
641	$\frac{7}{2}^-$	$\frac{5}{2}^-$	262	+0.19(17)			+3.7(3.3)
641	$\frac{7}{2}^-$				1.0(4)	0.4(2)	8(4)
942	$\frac{9}{2}^-$				0.57(25)	0.13(3)	2.9(7)
1325	$\frac{11}{2}^-$				<0.32	>0.27	<5

Woods-Saxon calculation [3], and from known moments [33]. For the $K = \frac{5}{2}$ positive parity band, based on the $g_{\frac{9}{2}}$ spherical orbital, the differences were quite small, at the few percent level; and for the $K = \frac{3}{2}$ negative parity band, mainly arising from $p_{\frac{3}{2}}$ spherical contributions, less than 10%. Uncertainties in the magnetic contribution thus have little effect on the following conclusions which are dominated by uncertainty in the extracted mixing ratios. For these particular orbits, there is also quite low sensitivity of $(g_K - g_R)$ to deformation. For example, the $[422]\frac{5}{2}^+$ orbit changes from $(g_K - g_R) = 0.893\,\mu_N$ at $\varepsilon_2 = +0.1$ to $(g_K - g_R) = 1.001\,\mu_N$ at $\varepsilon_2 = 0.4$. The mixing ratio, δ, is proportional to $(g_K - g_R)/Q$ (where Q is the quadrupole moment of the band) and Q scales with ε_2. To be precise, we infer the transitional quadrupole moments, which, in a fixed-shape strong-coupling analysis are equal to the intrinsic quadrupole moment of the band. Thus, in this specific case, the measurement of δ is tied to both the sign and the size of the deformation ε_2 in a rather model independent way.

For the positive parity band two mixing ratios are measured for the $\Delta I = 1$ transitions with $\frac{9}{2} \rightarrow \frac{7}{2}$ and $\frac{7}{2} \rightarrow \frac{5}{2}$. They are both positive in the convention of Krane and Steffen [28]. In this convention the sign of δ is proportional to the sign of $(g_K - g_R)/Q$. The g-factor is positive for all deformations, so the inferred quadrupole moment can only be positive. Thus, the band is prolate. To extract a multipole mixing ratio from the branching ratios we use the strong coupling model which assumes constant values of Q and K. We will discuss the reliability of this assumption later. Again, we will see that uncertainty in the experimental values far outweighs these imperfections in the analysis model. Three determinations of δ from branching ratios were possible, extending to spin $I^\pi = \frac{13}{2}^+$, and give results that are consistent with the results from angular distributions.

The situation for the negative parity band is similar. The g-factor is more sensitive to deformation, as it has significant $f_{\frac{5}{2}}$ (folded) and $p_{\frac{3}{2}}$ (stretched) contributions which play against each other. However, as the valence particle is a proton, the magnetic moments always come out large and positive. Again, the two extracted mixing ratios are positive (though with large uncertainties), so the deformation must be prolate. Four branching ratios give supporting mixing ratios.

Table II gives the mixing ratios and the inferred quadrupole moments. The data all point to large positive quadrupole deformation for the nucleus, with the positive parity band, arising from the $g_{\frac{9}{2}}$ intruder appearing more deformed. The experimental uncertainties are large in all cases, due to low statistics arising from the small production cross section for ^{83}Nb. The agreement between the mixing ratios extracted from branching ratios and from angular distributions is within the uncertainties. In the strong coupling limit where K is spin independent, for example in rare earth and actinide nuclei, the different approaches for inferring deformation agree well [34]. For many strongly-coupled cases in the $A \sim 80$ region, like ^{80}Y [35] and ^{73}Kr [36], and probably the ^{83}Nb negative parity band, reliable deformation parameters can be inferred from angular distribution data. However, in the specific cases of the $K = \frac{5}{2}^+$ bands in this region, the inferred deformations from angular distribution analysis appear to be systematically too large. In the branching ratio determination we can study the effect of rotational alignment changing K in the band, as the dominant effect arises from angular momentum coupling that alters the relevant Clebsch-Gordan coefficients. For example, in the positive parity band, if $K = \frac{5}{2}$ is constant, we infer $\delta = 0.18(2)$ for the $I = \frac{9}{2}$ level and thus $Q = 6.8(0.8)\ e$b (Table II). However, if the effective projection is reduced to $K = \frac{3}{2}$ in the $I = \frac{9}{2}$ state then $\delta = 0.09(1)$, still just consistent with the angular distribution value of $\delta = +0.15(6)$, but now inferring $Q = 3.4(0.4)\ e$b, much closer to expectations. A value of $K = \frac{1}{2}$ leads to inconsistency between the two methods. A similar inference can be drawn for the $I = \frac{11}{2}$ state where an effective $K = \frac{3}{2}$ value reduces Q

from the physically unrealistic value of 11(6) eb to 4.5(2.5) eb.

The mixing ratios and transition energies for ^{83}Nb are all very similar to the equivalent bands in ^{81}Y and ^{79}Rb. In the nearest isotone, ^{81}Y, which can be produced two orders of magnitude more prolifically, a direct comparison can be made between the extraction of Q from branching and mixing ratios with quadrupole moments determined directly from lifetime measurements. For ^{81}Y [37,38] and ^{79}Rb [39], direct lifetime determinations have led to the extraction of a transitional quadrupole moment of $Q \sim 3.6(3)\,e$b for the low spin members of the $K = \frac{5}{2}$ band, corresponding to a deformation of $\varepsilon_2 \sim 0.33$. It would be interesting, though difficult, to make a similar lifetime measurement for ^{83}Nb. For now, we conclude that Q is large and positive for both bands in ^{83}Nb, with deformation very similar to that of ^{81}Y.

IV. DISCUSSION

A. Systematic trends

The development of deformation in odd-A niobium isotopes can now be traced from ^{91}Nb at the $N = 50$ spherical shell closure down to deformed ^{83}Nb with $N = 42$, as depicted in the top row of Fig. 4. Initially, the positive parity states have $I = \frac{9}{2}$ as one would expect from the $g_{\frac{9}{2}}$ spherical state, with higher angular momentum states requiring pair-breaking, thus lying at >2 MeV. As the neutron number decreases, vibrational softness allows the $I = \frac{13}{2}$ state to fall below 1 MeV, but only below $N = 44$ does permanent deformation begin to develop and split the $g_{\frac{9}{2}}$ manifold into its Nilsson components. In ^{83}Nb the $[422]\frac{5}{2}^+$ Nilsson orbit has become the ground state, and a well deformed, strongly coupled band emerges.

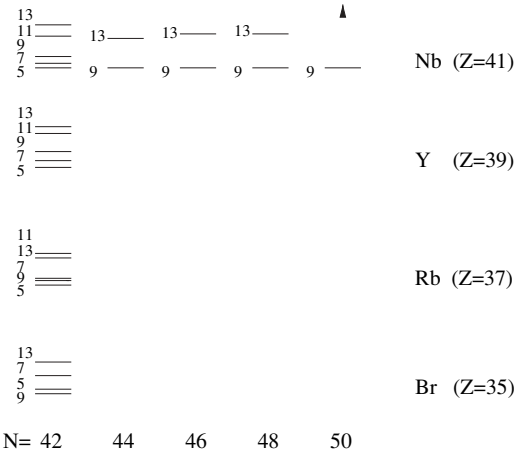

FIG. 4. Positive parity states below 1 MeV in odd-A niobium isotopes (top row) and $A \sim 80$, $N = 42$ isotones (leftmost column). Note that the states are labeled by twice their spin values ($2I$) for clarity of presentation. The states in the $N = 42$ isotones exhibit patterns characteristic of strongly coupled bands, while the niobium isotopes show a striking departure from this behavior for $N > 42$. Only in the $N = 42$ isotones does the large deformation allow the $g_{\frac{9}{2}}$ intruder orbital to descend and form strongly coupled bands.

This strongly coupled structure is present in all the $N = 42$ isotones in this region, as displayed in the leftmost column of Fig. 4. Indeed, in the $A \sim 80$ region, the trend from near-spherical, through vibrational-like, to stably deformed nuclei, seems to be very strongly dependent on neutron number, and almost all nuclei from krypton ($Z = 36$) to niobium ($Z = 41$) have the same neutron number dependence, with permanent deformation being found in nuclei with $N < 44$. As Fig. 4 illustrates, all of these odd-A niobium isotopes plus the $A \sim 80$, $N = 42$ isotones have levels built on the $g_{\frac{9}{2}}$ shell-model orbital, but only in the $N = 42$ isotones do strongly coupled band structures of both signatures ($\alpha = +\frac{1}{2}; I = \frac{5}{2} \ldots \frac{9}{2} \ldots \frac{13}{2}$) and ($\alpha = -\frac{1}{2}; I = \frac{7}{2} \ldots \frac{11}{2} \ldots \frac{15}{2}$) interleave and become well populated in experiment. This is a signature of stable deformation, and the $[422]\frac{5}{2}^+$ band head at the Fermi level is also consistent with a prolate shape.

The restriction of large prolate deformation to below neutron number $N = 44$, combined with the locus of the proton drip line [6], defines the tip of a triangle in the nuclear chart. For example, the next odd-Z isotone, ^{85}Tc also would be expected to be deformed but lies beyond the drip line.

B. Projected shell model calculations

Theoretical calculations were performed by using the projected shell model (PSM) [40], which uses deformed Nilsson single-particle states [32] as the model basis. Pairing correlations are incorporated into the Nilsson states by a BCS calculation. These Nilsson-BCS calculations define a set of quasiparticle (qp) states corresponding to the qp vacuum $|0\rangle$. One then constructs the shell model basis by building multi-qp states from those Nilsson orbitals that lie close to the Fermi levels. The broken rotational symmetry in the multi-qp states is recovered by exact angular momentum projection [41] to form a shell model basis in the laboratory frame. Finally, a two-body Hamiltonian is diagonalized in the projected space. The PSM wavefunction is in general a superposition of projected multi-qp states that span the shell model space given by

$$|\psi_M^I\rangle = \sum_\kappa f_\kappa^I \hat{P}^I_{\mathrm{MK}_\kappa} |\phi_\kappa\rangle. \quad (1)$$

In Eq. (1), κ labels the basis states and the f_κ^I amplitudes are determined by the configuration mixing implemented by the diagonalization. $\hat{P}^I_{\mathrm{MK}_\kappa}$ is the angular-momentum projection operator [41] which projects an intrinsic configuration $|\phi_\kappa\rangle$ onto states with good angular momentum. In this mass region, the valence space consists of protons and neutrons in three major shells ($N = 2, 3, 4$). $|\phi_\kappa\rangle$ consists of 0-, 2-, and 4-qp states:

$$|\phi_\kappa\rangle = \left\{|0\rangle, \alpha^\dagger_{n_i}\alpha^\dagger_{n_j}|0\rangle, \alpha^\dagger_{p_k}\alpha^\dagger_{p_l}|0\rangle, \alpha^\dagger_{n_i}\alpha^\dagger_{n_j}\alpha^\dagger_{p_k}\alpha^\dagger_{p_l}|0\rangle\right\}, \quad (2)$$

where $\alpha^\dagger$ is the creation operator for a qp and the index n (p) denotes neutron (proton) Nilsson quantum numbers which run over the orbitals close to the Fermi levels. In the PSM calculations, we employ a quadrupole plus pairing

Hamiltonian, with the inclusion of a quadrupole-pairing term

$$\hat{H} = \hat{H}_0 - \frac{1}{2}\chi\sum_{\mu}\hat{Q}^{\dagger}_{\mu}\hat{Q}_{\mu} - G_M\hat{P}^{\dagger}\hat{P} - G_Q\sum_{\mu}\hat{P}^{\dagger}_{\mu}\hat{P}_{\mu}. \quad (3)$$

In Eq. (3), $\hat{H}_0$ is the spherical single-particle Hamiltonian which contains a proper spin-orbit force. The monopole pairing strength G_M is taken to be $G_M = [18.0 - 14.4(N - Z)/A]/A$ for neutrons and $G_M = 18.0/A$ for protons. The quadrupole pairing strength G_Q is assumed, as usual, to be proportional to G_M, the proportionality constant being fixed to 0.16 in the present work. These pairing strengths are the same as the values used in previous PSM calculations (see, for example, Ref. [42]). Finally, the quadrupole-quadrupole interaction strength χ is determined by the self-consistent relation associated with the deformation ε_2 [40].

In principle, any deformation can be used to generate the basis states for the PSM calculations. However, the closer the chosen initial basis lies to the actual deformation, the less the influence of configuration mixing, and the simpler the calculation and interpretation. To describe the level spacings and alignments, a basis with $\varepsilon_2 = 0.28$, $\varepsilon_4 = 0.0$ ($\beta_2 = 0.3$) was found to provide the best reproduction of the data. This is lower than inferred from the electromagnetic decays. For now, we can employ the reduced-deformation basis to interpret the structure of ^{83}Nb. In the experimental level scheme in Fig. 2, one rotational band with positive parity and another with negative parity are grouped into $\Delta I = 2$ sequences according to the signature quantum number. For an odd mass nucleus, the energetically favored branch takes $I = j \pmod 2$ while the unfavored one has $I = j + 1 \pmod 2$, where j is the angular momentum carried by the last nucleon.

In the $A \sim 80$ region, prolate-oblate shape coexistence is often an important topic. One key question is whether the observed data in ^{83}Nb could be associated with an oblate deformation. The analysis of mixing ratios, discussed earlier, firmly points to prolate deformation for both bands. To investigate this aspect theoretically, we have performed a calculation by constructing a basis at $\varepsilon_2 = -0.28$, $\varepsilon_4 = 0.0$. It was found that in this case, the lowest proton 1-qp band has $K = \frac{7}{2}^+$. Although this K value is not completely excluded for the experimental positive parity band, systematic trends make it appear unlikely. Further, the oblate calculations do not reproduce the features of the band very well, supporting a prolate solution with $K = \frac{5}{2}^+$. The following results were calculated with a prolate basis deformation of $\varepsilon_2 = 0.28$.

To account for the variations in the moments of inertia and to further understand the structure of the bands, we first present the band diagrams in Figs. 5 and 6. A band diagram in the PSM contains selected rotational sequences in their pure configurations. In this way, it is easy to identify which configurations are of greatest interest. The dots in Figs. 5 and 6 represent the lowest states at each spin obtained after band mixing, and these are the theoretical points which are compared with experimental data in the plots of the moments of inertia (see Figs. 7 and 8).

It can be seen that signature splitting occurs between the two partners of the positive band. Signature splitting phenomena in odd-mass nuclei have been studied in the PSM framework in

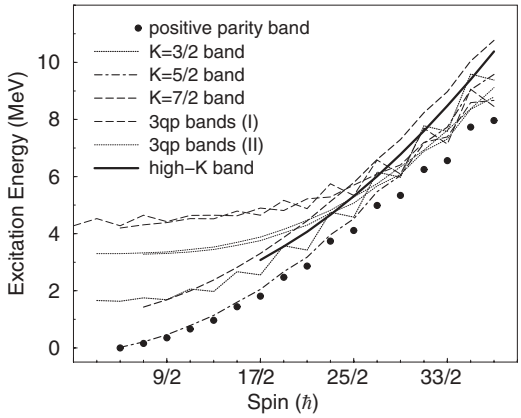

FIG. 5. A band diagram calculated in the PSM showing the lowest positive parity states and their evolution with spin. The dots in this diagram represent the calculated yrast sequence which arises from mixing the pure Nilsson bands.

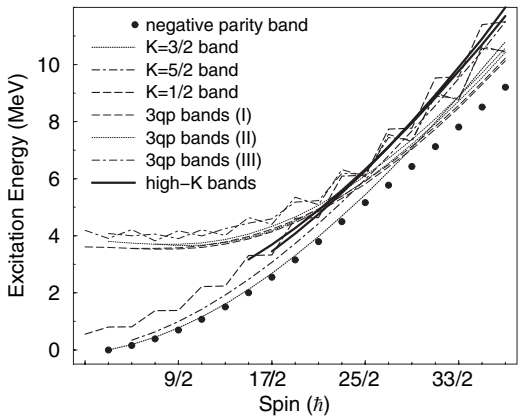

FIG. 6. A band diagram similar to Fig. 5, but calculated for negative parity states.

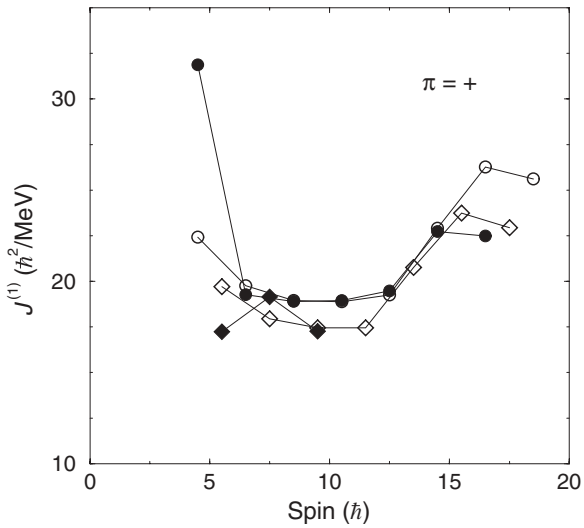

FIG. 7. The moments of inertia calculated (open symbols) for the positive parity band and compared to data (filled symbols). The circles correspond to the positive signature states, and the diamonds to the negative signature states.

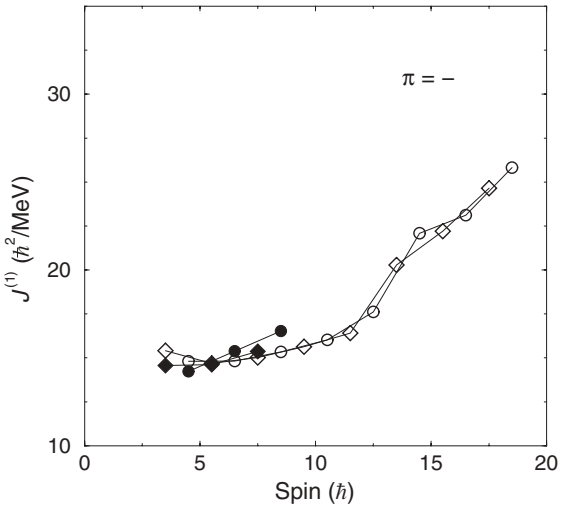

FIG. 8. The calculated (open symbols) and experimental (filled symbols) moments of inertia for the negative parity bands in ^{83}Nb. The circles correspond to the positive signature, and the diamonds to the negative signature.

Refs. [43,44]. In Figs. 7 and 8, the lowest bands obtained in the calculations, with positive and negative parity, are compared respectively with the data presented in the form of moment of inertia (defined as $J^{(1)}(I) = (2I - 1)/[E(I) - E(I - 2)]$) versus spin. It can be seen from both figures that the theory reproduces the data very well. One exception is the first data point in Fig. 7 for the positive parity band. However, we note that the present calculation is not the only case having this discrepancy; a similar one has been seen in several other $N \approx Z$ calculations [23]. A possible source for this discrepancy is that the model does not fully incorporate the effects of neutron-proton pairing, whose influence is usually present in the low-spin, low-excitation region in $N \approx Z$ nuclei.

For the positive parity states in Fig. 5, we found that the proton 1-qp band based on the $[422]\frac{5}{2}^+$ state lies lowest in energy in the low-spin region while the other two, the $[431]\frac{3}{2}^+$ and $[413]\frac{7}{2}^+$ bands, lie about 1.5 MeV higher in excitation energy. Thus the main component in the positive parity band under discussion should have $K = \frac{5}{2}$. However, the band cannot retain this pure configuration when the nucleus rotates faster because the other configurations are seen to come down approaching, or even crossing, the $K = \frac{5}{2}$ band at higher spins. The sequence with the zig-zag behavior, i.e., the $[431]\frac{3}{2}^+$ band, influences the results strongly. This zig-zag behavior shown in the band diagram corresponds to a splitting between the two signature partners, a phenomenon that typically occurs only for configurations with smaller K values. The strong mixing with the $K = \frac{3}{2}$ configuration explains the observed signature splitting after band mixing occurs, since the dots in Fig. 5 do not form a smooth curve but instead show a clear stepwise pattern. Therefore, the slopes of the two signature branches (if one connects the dots separately for the two branches in Fig. 5) are different. A greater slope of a curve in an E-I plot is associated with a faster rotation and, due to angular momentum conservation in the system, the corresponding moment of inertia must be smaller. As can be seen in Fig. 7, the unfavored branch has indeed a smaller moment of inertia than the favored one. Thus the observables are well described by the theory, which provides an example of signature partners with different moments of inertia that nevertheless have the same intrinsic structure.

TABLE III. Major amplitudes of the wave functions for the positive parity states displayed in Fig. 5.

Parity	qps	Total K	Configurations
+	1-qp	5/2	π 5/2[422]
		7/2	π 7/2[413]
		3/2	π 3/2[431]
	3-qp	3/2	$\pi 5/2[422] \oplus \nu 3/2[431] \oplus \nu 5/2[422]$
		7/2	$\pi 5/2[422] \oplus \nu 3/2[431] \oplus \nu 5/2[422]$
		1/2	$\pi 3/2[431] \oplus \nu 3/2[431] \oplus \nu 5/2[422]$
		5/2	$\pi 3/2[431] \oplus \nu 3/2[431] \oplus \nu 5/2[422]$
	3-qp	17/2	$\pi 5/2[422] \oplus \nu 5/2[422] \oplus \nu 7/2[413]$

At about $I = \frac{25}{2}$, a group of 3-qp bands comes down in energy, interacts with and eventually crosses the 1-qp bands, to become yrast. Among the 3-qp bands, the most important ones are listed in Table III. The corresponding wave functions must undergo a configuration change due to band mixing. This change in configuration can lead to observable consequences. In fact, the current data show a sudden increase in the moment of inertia starting at $I = \frac{25}{2}$ (see Fig. 7). In contrast, most of the variations discussed above are not seen in the negative parity band. As shown in Fig. 8, the two branches of the negative signature partners have the same moments of inertia. In the corresponding band diagram in Fig. 6, the lowest band is the proton 1-qp $[301]\frac{3}{2}^-$ band. The $[301]\frac{1}{2}^-$ band lies about 1 MeV above it. However, unlike the positive parity case, the $K = \frac{1}{2}$ band, with a clear zigzag behavior, does not mix with the $K = \frac{3}{2}$ band. No signature splitting in the $K = \frac{3}{2}$ band is thus observed. The reason for this is that the $K = \frac{1}{2}$ band originates from the $p_{\frac{1}{2}}$ orbital, and does not interact with the $K = \frac{3}{2}$ band, which belongs to a different orbital. At $I = \frac{25}{2}$, the calculation predicts a similar upbending in moment of inertia as in the positive parity case, due to the bandcrossing with the 3-qp states (listed in Table IV).

TABLE IV. Major amplitudes of the wave functions for negative parity configurations displayed in Fig. 6.

Parity	qps	Total K	Configurations
−	1-qp	3/2	π 3/2[301]
		5/2	π 5/2[303]
		1/2	π 1/2[301]
	3-qp	1/2	$\pi 3/2[301] \oplus \nu 3/2[431] \oplus \nu 5/2[422]$
		5/2	$\pi 3/2[301] \oplus \nu 3/2[431] \oplus \nu 5/2[422]$
		3/2	$\pi 5/2[303] \oplus \nu 3/2[431] \oplus \nu 5/2[422]$
		7/2	$\pi 5/2[303] \oplus \nu 3/2[431] \oplus \nu 5/2[422]$
		1/2	$\pi 1/2[301] \oplus \nu 3/2[431] \oplus \nu 5/2[422]$
		3/2	$\pi 1/2[301] \oplus \nu 3/2[431] \oplus \nu 5/2[422]$
	3-qp	17/2	$\pi 5/2[303] \oplus \nu 5/2[422] \oplus \nu 7/2[413]$
		15/2	$\pi 3/2[301] \oplus \nu 5/2[422] \oplus \nu 7/2[413]$

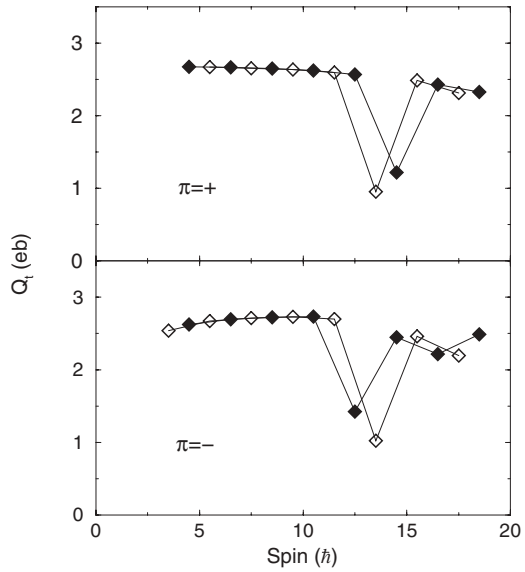

FIG. 9. The calculated transition quadrupole moments as a function of spin for both signatures of the positive parity (upper panel) and negative parity (lower panel) states in ^{83}Nb. A deformation of $\varepsilon_2 = +0.28$ was used for the Nilsson basis states.

Three quasiparticle high-K band heads are predicted of both positive and negative parity (see Figs. 5 and 6 and Tables III and IV). A positive parity band head with $I^\pi = K^\pi = \frac{17}{2}^+$ is predicted to lie at 3057 keV, or 1336 keV above the yrast $I^\pi = \frac{17}{2}^+$ state with $K = \frac{5}{2}$. Thus, the decay would be a mixed $E2/M1$ transition involving a change of K by $6\hbar$. The reduced degree of hindrance for this kind of transition in heavier nuclei [45,46] is 10–70, indicating the isomer would have a lifetime in the several nanosecond to several microsecond regime. The lifetimes of the high-K negative parity band heads with $I^\pi = K^\pi = \frac{15}{2}^-$ and $\frac{17}{2}^-$, predicted to lie at 3133- and 3370-keV, respectively, are more difficult to estimate, as all $E1$ decays are inhibited; but these isomers could also be in the nanosecond regime. The observation of such isomers would provide a discriminating test of K-quantum number violation; that is, how near the nucleus is to a stiff axial shape. Unfortunately, the technique employed in this study, using a thin target from which reaction products escape at high velocity, is very restrictive for isomer searches, as the excited nuclei move away from the center of Gammasphere in a few nanoseconds and thus prevent the detection of delayed γ rays. These time ranges are amenable to electronic timing and beam-chopping techniques. More sensitive isomer searches are being considered.

The transition quadrupole moments can be calculated as a function of spin. The quadrupole moment Q_t is defined as

$$Q_t(I,K) = \sqrt{\frac{16\pi}{5}}\frac{\sqrt{B(E2: I, K \to I-2, K)}}{\langle I, K, 2, 0 | I-2, K\rangle}, \quad (4)$$

where the $B(E2)$ values are calculated as

$$B(E2, I_i \to I_f) = \frac{1}{2I_i+1}|\langle \psi^{I_f}||\hat{Q}_2||\psi^{I_i}\rangle|^2. \quad (5)$$

Standard values for the effective charge are used in the calculation, i.e., $e_\pi = 1.5e$ and $e_\nu = 0.5e$. It is found that the calculated Q_t for both positive and negative parity bands have rather similar values at low spins although they show slightly different trends, as seen in Fig. 9. At higher spins, and in particular after the 1-qp and 3-qp band crossings, Q_t clearly decreases. This decrease in transition quadrupole moment corresponds to a quenching of deformation. The drop in Q_t at spins $I = \frac{27}{2}$ and $\frac{29}{2}$ for the positive parity bands, and at $I = \frac{25}{2}$ and $\frac{27}{2}$ for the negative parity bands, is attributed to the sudden change in the content of the wave function (from 1-qp states as main component to 3-qp states) due to band mixing, as discussed above.

Not surprisingly, the calculated quadrupole moments are smaller than those inferred from experiment, due to the chosen basis. However, rescaling the ratio of the model deformation ($\varepsilon_2 = 0.28$) and experimental expectations ($\varepsilon_2 = 0.33$) brings excellent agreement. The predicted trends in transitional quadrupole moments are interesting, with a sharp drop at the transition to three quasiparticle states. Measuring lifetimes in the up-bending region would clearly be discriminating.

V. CONCLUSIONS

^{83}Nb has been studied in detail. Two well developed rotational bands have been delineated, building on the pioneering observations of Gross *et al.* [19]. The new data allow both bands to be categorized as arising from rotation of a shape associated with large prolate deformation. Among other issues, this firmly points to a $I^\pi = \frac{5}{2}^+$ ground state assignment. The size of the deformation appears to be close to that of other $N = 42$ isotones, such as ^{81}Y, which can be much more strongly produced and have been shown to have $\varepsilon_2 \sim 0.33$. Most of the experimentally observed features could be reproduced using the projected shell model, which provides insight into the shape and mixing of configurations, although a basis deformation smaller than suggested by experiment was necessary. This nucleus likely represents the upper limit to such large deformation in this region. Even the addition of one proton in ^{84}Mo makes the nucleus softer and more vibrational-like, while the next odd-Z isotone, ^{85}Tc lies beyond the proton drip line.

ACKNOWLEDGMENTS

We would like to thank the members of the Argonne support group who keep Gammasphere in good operational condition. This research was supported in part by the DOE Office of Nuclear Physics under contracts W-ENG-109-38 and FG02-88ER-40406, by a Research Corporation grant CC5166, and by NSF grants PHY95-14157 and PHY-0244895. Y.S. is partly supported by the NSF under contracts PHY-0140324 and PHY-0216783.

[1] E. K. Warburton, J. W. Olness, C. J. Lister, R. W. Zurmuhle, and J. A. Becker, Phys. Rev. C **31**, 1184 (1985).
[2] C. J. Lister, M. Campbell, A. A. Chishti, W. Gelletly, L. Goettig, R. Moscrop, B. J. Varley, A. N. James, T. Morrison, H. G. Price, J. Simpson, K. Connel, and O. Skeppstedt, Phys. Rev. Lett. **59**, 1270 (1987).
[3] W. Nazarewicz, J. Dudek, R. Bengtsson, T. Bengtsson, and I. Ragnarsson, Nucl. Phys. **A435**, 397 (1985).
[4] A. Harder *et al*., Phys. Rev. C **55**, 1680 (1997).
[5] T. Faestermann *et al*., Eur. Phys. J. A **15**, 185 (2002).
[6] Z. Janas *et al*., Phys. Rev. Lett. **82**, 295 (1999).
[7] P. Möller and J. R. Nix, At. Nucl. Data Tables **26**, 1965 (1981).
[8] S. Åberg, Phys. Scr. **25**, 23 (1982).
[9] W. Gelletly, M. A. Bentley, H. G. Price, J. Simpson, C. J. Gross, J. L. Durell, B. J. Varley, O. Skeppstedt, and S. Rastikerdar, Phys. Lett. **B253**, 287 (1991).
[10] N. Marginean *et al*., Phys. Rev. C **65**, 051303(R) (2002).
[11] N. Marginean, Eur. Phys. J. A **20**, 123 (2004).
[12] D. Rudolph *et al*., Phys. Rev. C **54**, 117 (1996).
[13] J. Garces Narro *et al*., Phys. Rev. C **63**, 044307 (2001).
[14] C. J. Gross, W. Gelletly, M. A. Bentley, H. G. Price, J. Simpson, K. P. Lieb, D. Rudolph, J. L. Durell, B. J. Varley, and S. Rastikerdar, Phys. Rev. C **44**, R2253 (1991).
[15] K. Jonsson *et al*., Nucl. Phys. **A645**, 47 (1999).
[16] K. Lagergren and B. Cederwall, Eur. Phys. J. A **21**, 175 (2004).
[17] C. Chandler *et al*., Phys. Rev. C **61**, 044309 (2000).
[18] P. H. Regan *et al*., Proceedings of Nucleus-Nucleus Conference, Rio de Janeiro, Brazil, 2006, to be published in Nucl. Phys. A (2007).
[19] C. J. Gross, W. Gelletly, M. A. Bentley, H. G. Price, J. Simpson, B. J. Varley, J. L. Durell, O. Skeppstedt, and S. Rastikerdar, Phys. Rev. C **43**, R5 (1991).
[20] M. Wiescher and H. Schatz, Nucl. Phys. **A693**, 269 (2001).
[21] Yu. Novikov *et al*., Eur. Phys. J. A **11**, 257 (2001).
[22] H. Schatz, A. Aprahamian, V. Barnard, L. Bildsten, A. Cumming, M. Ouellette, T. Rauscher, F.-K. Thielemann, and M. Wiescher, Phys. Rev. Lett. **86**, 3471 (2001).
[23] Y. Sun, Eur. Phys. J. A **20**, 133 (2004).
[24] Y. Sun, M. Wiescher, A. Aprahamian, and J. Fisker, Nucl. Phys. **A758**, 765c (2005).
[25] I. Y. Lee, Nucl. Phys. **A520**, 641c (1990).
[26] C. N. Davids, B. B. Back, K. Bindra, D. J. Henderson, W. Kutschera, T. Lauritsen, Y. Nagame, P. Sugathan, A. V. Ramayya, and W. B. Walters, Nucl. Instrum. Methods Phys. Res. B **70**, 358 (1992).
[27] T. Kuroyanagi, S. Mitarai, B. J. Min, H. Tomura, Y. Haruta, K. Heiguchi, and S. Suematsu, Nucl. Phys. **A484**, 264 (1988).
[28] K. S. Krane, R. M. Steffen, and R. M. Wheeler, Nucl. Data Tables **11**, 351 (1973).
[29] H. Morinaga and T. Yamazaki, *In-Beam Gamma Spectroscopy* (North Holland, Amsterdam, 1976), p. 353.
[30] K. Nakai, Phys. Lett. **B34**, 269 (1971).
[31] S. G. Nilsson, Mat. Fys. Medd. Dan. Vid. Selsk. Vol. **29** No. 16 (1952).
[32] T. Bengtsson and I. Ragnarsson, Nucl. Phys. **A436**, 14 (1985).
[33] National Nuclear Data Center, www.nndc.bnl.gov (2006).
[34] A. Bohr and B. R. Mottelson, *Nuclear Structure* (W.A. Benjamin, Inc., New York, 1975), Vol. II.
[35] D. Bucurescu *et al*., Nucl. Phys. **A705**, 3 (2002); J. Ressler, Ph.D. thesis, University of Maryland, 2000 (unpublished).
[36] N. Kelsall *et al*., Phys. Rev. C **65**, 044331 (2002)
[37] R. A. Kaye *et al*., Phys. Rev. C **66**, 054305 (2002).
[38] T. D. Johnson, A. Raguse, C. J. Gross, M. K. Kabadiyski, K. P. Lieb, D. Rudolph, M. Weiszflog, T. Burkardt, J. Eberth, and S. Skoda, Z. Phys. A **350**, 189 (1994).
[39] M. J. Leddy, J. L. Durell, S. J. Freeman, B. J. Varley, R. A. Bark, C. D. O'Leary, and S. Tormanen, Phys. Rev. C **58**, 1438 (1998).
[40] K. Hara and Y. Sun, Int. J. Mod. Phys. E **4**, 637 (1995).
[41] P. Ring and P. Schuck, *The Nuclear Many Body Problem* (Springer-Verlag, New York, 1980).
[42] Y. Sun and J. A. Sheikh, Phys. Rev. C **64**, 031302(R) (2001).
[43] K. Hara and Y. Sun, Nucl. Phys. **A537**, 77 (1992).
[44] Y. Sun, D. H. Feng, and S. Wen, Phys. Rev. C **50**, 2351 (1994).
[45] K. E. G. Lobner, Phys. Lett. **B26**, 369 (1968).
[46] M. Dasgupta, G. D. Dracoulis, P. M. Walker, A. P. Byrne, T. Kibedi, F. G. Kondev, G. J. Lane, and P. H. Regan, Phys. Rev. C **61**, 044321 (2000).